Strong and selective magnon-phonon coupling in the van der Waals antiferromagnet $CoPS_3$

Dipankar Jana,[1,2,*] Diana Vaclavkova,[1] Rajesh Kumar Ulaganathan,[3] Raman Sankar,[3] Milan Orlita,[1,4] Clement Faugeras,[1] Maciej Koperski,[2,5] M. E. Zhitomirsky,[6,7] and Marek Potemski[1,8,9,†]

[1]*Laboratoire National des Champs Magnétiques Intenses, LNCMI-EMFL, CNRS UPR3228, Université Grenoble Alpes, Université Toulouse, Université Toulouse 3, INSA-T, Grenoble, France*

[2]*Institute for Functional Intelligent Materials, National University of Singapore, 117544 Singapore*

[3]*Institute of Physics, Academia Sinica, Taipei 10617, Taiwan*

[4]*Institute of Physics, Charles University, Ke Karlovu 5, Prague 121 16, Czech Republic*

[5]*Department of Materials Science and Engineering, National University of Singapore, 117575 Singapore*

[6]*Université Grenoble Alpes, CEA, Grenoble INP, IRIG, Pheliqs, 38000 Grenoble, France*

[7]*Institut Laue-Langevin, 38042 Grenoble Cedex 9, France*

[8]*CENTERA, CEZAMAT, Warsaw University of Technology, 02-822 Warsaw, Poland*

[9]*Institute of High Pressure Physics, PAS, 01-142 Warsaw, Poland*

(Received 5 July 2025; revised 24 September 2025; accepted 26 September 2025; published 24 October 2025)

The Raman scattering response of the biaxial antiferromagnet $CoPS_3$ has been investigated as a function of both magnetic field and temperature. The peaks observed in the low-frequency spectral range (90–200 cm^{-1}) have been identified as hybrid magnon-phonon excitations. The energies of the bare magnon and phonon modes and the effective coupling strengths between different excitation pairs have been determined. The strong and selective magnon-phonon interaction largely accounts for the pronounced splitting of two phononlike modes observed at 152 and 158 cm^{-1} in the antiferromagnetic phase of $CoPS_3$. Based on the identification of bare magnon excitations and their magnetic-field dependence, we propose an updated set of parameters for the effective exchange ($J_{\rm eff} = 9.9$ meV) and biaxial magnetic anisotropy ($D = 4.3$ meV and $E = -0.7$ meV) and advocate for an apparent anisotropic g factor ($g_x = g_y = 2$, $g_z = 4$) in the $CoPS_3$ antiferromagnet.

DOI: 10.1103/8f92-lt57

I. INTRODUCTION

The interplay between lattice vibrations (phonons) and spin-wave excitations (magnons) in magnetic materials has attracted significant attention due to its fundamental importance and potential applications in fields such as spintronics, magnonics, and quantum information processing [1–11]. Investigating magnon and phonon excitations—and their possible hybridization—is particularly compelling in van der Waals (vdW) magnets, especially antiferromagnets [8,12–21]. These materials are of interest not only from a fundamental perspective, particularly in the strictly two-dimensional (2D) limit, but also from an applied standpoint. In magnetically anisotropic vdW antiferromagnets, magnons are gapped excitations (with finite energy at $k = 0$), and these magnon gaps often lie at sufficiently high energies near optical phonon modes [15–18]. Such systems are especially relevant for terahertz technologies, potentially at micro- and nanoscale dimensions. This is particularly the case when these magnons couple to optically active phonon modes, enabling efficient manipulation and detection of spin-lattice dynamics and, possibly, tunability of the modes' amplitude and/or frequency [15,20,22]. Coupling between $k = 0$ magnon and phonon modes, resulting in the formation of magnon-polarons, was already demonstrated in iron-based vdW antiferromagnets such as $FePS_3$ and $FePSe_3$, where magnon and phonon excitations nearly coincide in energy [14–16,19–21]. Crucially, the identification of this coupling relies on detecting characteristic mode repulsion when effectively tuning the $k = 0$ magnonlike mode via applied magnetic fields. Magnon and phonon modes are also expected to nearly coincide in the cobalt-based vdW antiferromagnet $CoPS_3$ [23], making it another candidate for exploring magnon-phonon interactions.

Spin ordering and dynamics in $CoPS_3$ have been extensively investigated through magnetometry and a series of inelastic neutron scattering studies of this antiferromagnet [23–26]. In the magnetically ordered phase, Co^{2+} spins ($S = 3/2$) are arranged on a honeycomb lattice, forming zigzag ferromagnetic chains along the a axis. These chains are antiferromagnetically coupled along the b axis (see Fig. 1). The magnetic moments are predominantly aligned along the crystallographic a axis, although a slight out-of-plane canting of about 10° has also been suggested [24]. The theoretical modeling of the spin-wave dispersion has evolved over time [23–26]. The most recent and comprehensive model is based on a two-dimensional spin-3/2 Hamiltonian that incorporates isotropic exchange interactions J_{ij} up to third-nearest neighbors in the ab plane, as well as biaxial single-ion anisotropy described by two parameters, D and E [26,28]:

$$\hat{\mathcal{H}} = \sum_{\langle ij \rangle} J_{ij} \mathbf{S}_i \cdot \mathbf{S}_j + \sum_i \left\{ D\left(S_i^z\right)^2 + E\left[\left(S_i^x\right)^2 - \left(S_i^y\right)^2\right]\right\}. \quad (1)$$

*Contact author: jana.d02@nus.edu.sg
†Contact author: marek.potemski@lncmi.cnrs.fr

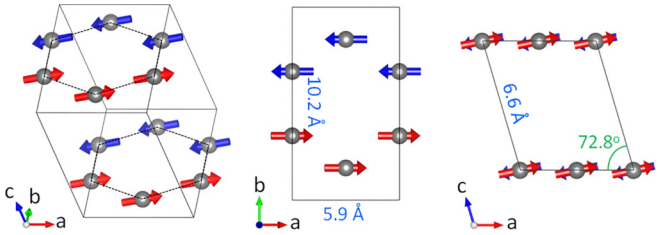

FIG. 1. Magnetic structure of $CoPS_3$ in the antiferromagnetic phase, shown in different crystallographic planes. Gray spheres denote Co^{2+} ions, while red and blue arrows indicate the spin orientations of the two sublattices. The monoclinic crystal structure (space group $C2/m$) and unit cell parameters are also illustrated [24]. Co^{2+} spins exhibit a slight out-of-plane canting [23]. This figure was generated using the VESTA software package [27].

Here, the x and y axes are defined along the crystallographic a and b directions, respectively, while z is oriented perpendicular to the ab plane (i.e., along the c^* axis). This model reproduces well the spin-wave dispersion observed in $CoPS_3$ single crystals by setting a ferromagnetic first-neighbor exchange ($J_1 = -1.37$ meV), antiferromagnetic second-neighbor exchange ($J_2 = 0.09$ meV), and strong antiferromagnetic third-neighbor exchange ($J_3 = 3.0$ meV). The anisotropy parameters are determined to be $D = 6.07$ meV and $E = -0.77$ meV, favoring the in-plane spin alignment along the x direction (i.e., the a axis), consistent with $D > 0$ and $E < 0$. Notably, the magnon spectrum of $CoPS_3$ appears to be gapped (finite excitation energy at $k = 0$). Two low-energy magnon gaps, characteristic for a biaxial antiferromagnet, have been estimated at 14 and 24 meV. While the 2D model effectively accounts for the inelastic neutron scattering data, it may still offer an incomplete description; nevertheless, recent estimates indicate that the interlayer exchange interactions are comparatively weak [26].

The bulk as well as a few layers and monolayers of the $CoPS_3$ antiferromagnet were also recently investigated with Raman scattering experiments focused on specific phonon modes [29]. The key reported observation was that a doubly degenerate phonon mode (at around 150 cm^{-1}) due to the in-plane vibration of cobalt atoms was observed to split into two components when the temperature was lowered below the Néel temperature ($T_N = 120$ K). This effect, tentatively attributed to an anticipated crystal lattice modification induced by spin ordering, has been used to trace the paramagnetic to antiferromagnetic phase transition in $CoPS_3$ specimens down to a monolayer.

Crucially, to date, little is known about the potential significance of magnon-phonon hybridization in this antiferromagnet. This omission is particularly noteworthy given the analogies between $CoPS_3$ and Fe-based layered antiferromagnets ($FePS_3$ and $FePSe_3$). As in $CoPS_3$, the Fe-based antiferromagnets display magnon excitations near phonon modes, with clear evidence of magnon-phonon hybridization effects [15–18].

In this paper, we report a Raman scattering study of low-energy excitations (in the spectral range of 90–200 cm^{-1}) in the van der Waals antiferromagnet $CoPS_3$. The measurements were performed as a function of the magnetic field, applied along different crystallographic directions, and as a function of temperature. In addition to the previously reported phononlike excitations, we identify two additional Raman peaks consistent with zone-center ($k = 0$) magnon-type modes. All observed features are interpreted as arising from coupled magnon-phonon excitations. By analyzing their evolution with magnetic field and temperature, we extract characteristic coupling strengths and determine the energies of the uncoupled (bare) magnon and phonon modes. In particular, we find that the coupling involving a nearly degenerate phonon doublet, centered around 157 cm^{-1}, is exceptionally strong and selective: One component of the doublet hybridizes with the lower-energy magnon, while the other couples to the higher-energy magnon. Notably, the phonon doublet, nearly degenerate in the uncoupled case, becomes distinctly split as a result of the hybridization with magnon modes. Based on the extracted bare magnon-gap energies and their magnetic-field evolution, we propose an updated set of exchange interaction and magnetic anisotropy parameters for $CoPS_3$. Furthermore, our results point to a strongly anisotropic g factor in this van der Waals antiferromagnet.

II. EXPERIMENTAL DETAILS

The $CoPS_3$ single crystals were grown by the chemical vapor transport method, using iodine as a transport agent. Initially, the polycrystalline powders were synthesized by a solid-state synthesis process under high-vacuum conditions. The high-purity starting materials, cobalt powder (99.999%), phosphorus powder (99.999%), and sulfur powder (99.999%), were weighted at a stoichiometric ratio and sealed into a quartz tube with a diameter of 22 mm with 10^{-3} Torr pressure. The mixed compounds were heated and grained twice at 400 °C and 600 °C to make a single-phase compound. Then 200 mg of iodine were added to the polycrystalline samples and sealed by a tube with dimensions of $20 \times 22 \times 400$ mm^3 at 10^{-3} Torr. The tube was kept for growth in a two-zone furnace with temperatures of 700 °C and 600 °C for 200 h. After the growth process was complete, the temperature of the furnace was reduced to room temperature at a rate of 2 °C/min. The quartz tube was broken inside an argon-filled glovebox, and the crystals were collected. A bulk crystal with dimensions of $\sim 2 \times 2 \times 0.2$ mm^3 was glued on a silicon substrate, and the top layer was removed using Scotch tape to eliminate degraded surface layers. Then it was placed either onto a cold finger of a helium flow cryostat for temperature-dependent measurements or inside a liquid-helium-cooled homemade setup for magneto-optical investigations, where the resistive magnet can reach 30 T.

Micro-optical setups were used to perform Raman scattering measurements as a function of temperature in zero magnetic field, as well as at low temperature (5 K) under externally applied magnetic fields oriented either perpendicular to the sample plane (out-of-plane geometry) or parallel to it (in-plane geometry). A continuous wave semiconductor-based laser operating at a wavelength of $\lambda = 515$ nm was focused on the sample with a microscope objective with a numerical aperture of 0.5 (helium flow cryostat) or 0.83 (magneto-Raman measurements). The scattered signals were collected using the same objective, dispersed with a 0.7 m long monochromator with 2000 L/mm grating, and detected

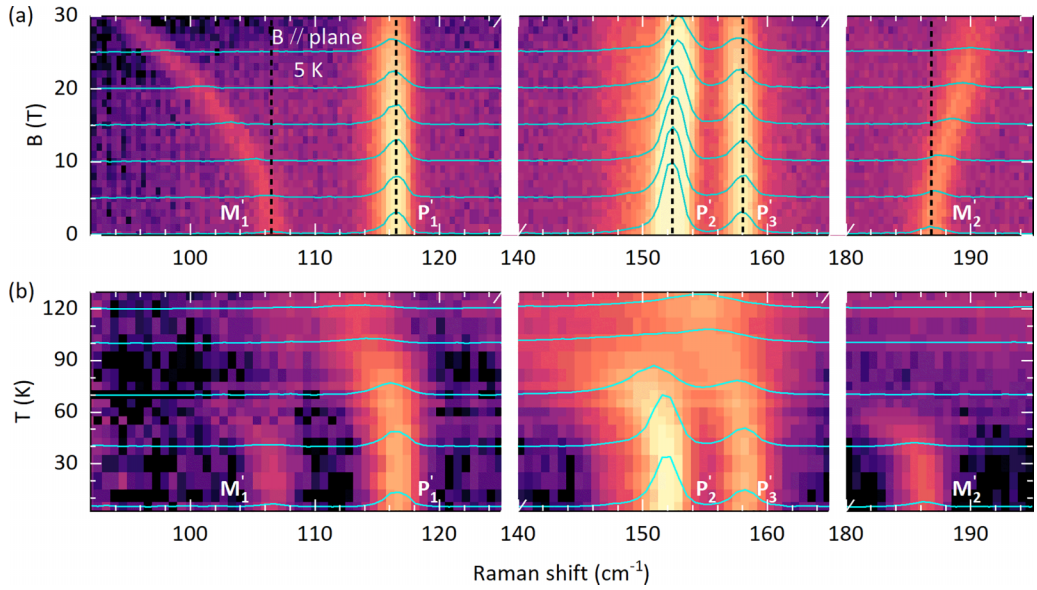

FIG. 2. False-color map of the Raman scattering response of the $CoPS_3$ antiferromagnet together with selected characteristic spectra. The coupled magnonlike modes are labeled M_i', while the phononlike modes are labeled P_i'. (a) Low-temperature (5 K) data collected as a function of the magnetic field B, applied conceivably along the in-plane crystal a axis. Vertical dashed lines are drawn at the central energies of the phononlike features measured at zero magnetic field. This is to emphasize the sensitivity, although weak, of the P_i' modes to the applied magnetic field. Common red or blue B shifts for different pairs of P_i' and M_i' modes point out the repulsion and thus selective coupling of M_1' with P_1' and P_3' but M_2' with P_2'. (b) Evolution of M_i' and P_i' modes with temperature (at $B = 0$ T). Redshifts and softening of M_i' modes underline their magnonlike character.

with a nitrogen-cooled charge-coupled device camera. A set of reflection-based Bragg filters was used in both the excitation and collection paths to clean the laser line and reject the backscattered laser. For the magneto-Raman scattering experiments in the in-plane geometry, the orientation of the magnetic field relative to the spin alignment (a axis) is particularly relevant. However, the crystallographic orientation of our small-size "samples" (essentially limited in size to the laser spot and the penetration depth) could not be determined with certainty, partly due to possible twinning along the c axis [23]. Consequently, we investigated different in-plane field configurations by performing multiple magnetic-field scans, applying the field parallel, perpendicular, or at 30° and 60° relative to a selected crystal edge, which is assumed to correspond to a specific crystallographic axis (see Fig. S2 in the Supplemental Material (SM) for four representative scans [30]). Regions with nearly uniform spin orientation (within the laser penetration depth), which enabled clear observation of distinct magnon field dependences, were identified by careful positioning of the laser spot on the sample. Nevertheless, in the dataset shown in Fig. S2(b), the coexistence of domains with different spin orientations could not be avoided, as evidenced by the observed branching of the high-energy magnon mode. Relevant configurations, with magnetic field applied (nearly) along or perpendicular to the spin alignment direction (a and b axes, respectively), were identified *a posteriori* by comparison with the different theoretically expected magnon field dependences.

III. EXPERIMENTAL RESULTS AND DISCUSSION

Magnons (spin waves) and phonons are two characteristic low-energy excitations in antiferromagnets that, in the limit of zero wave vectors ($k = 0$), can be effectively traced using Raman scattering experiments, especially when external parameters such as temperature and magnetic field are varied.

Our Raman scattering experiments on $CoPS_3$ crystals mainly focus on excitations at relatively low energies in the spectral range of 90–200 cm^{-1}. Two representative datasets are illustrated in Fig. 2. Spectra measured at the base temperature ($T = 5$ K) as a function of the applied magnetic field, $B = 0$–30 T, are shown in Fig. 2(a), whereas the spectral evolution with temperature, $T = 5$–130 K, in the absence of the magnetic field is presented in Fig. 2(b) (see Fig. S1(a) of the SM [30] for Raman scattering over a broad spectral range). As mentioned above, we carried out the magneto-Raman scattering experiments in various configurations of the field directions relative to the sample edges; the spectral evolution with the magnetic field changes for different configurations (see Fig. S2 of the SM [30]). The data presented in Fig. 2(a) were specifically selected for their most pronounced spectral changes in response to the magnetic field. As discussed below, this dataset corresponds most closely to the configuration of the magnetic field applied in the plane, along the crystal a axis, i.e., the spin alignment direction.

Focusing on the basic spectra (at $T = 5$ K, $B = 0$ T), we first recognize the characteristic Raman peaks, labeled here as P_1', P_2', and P_3', which were previously observed and assigned to phonon-type excitations [29]. Overlooked in previous Raman scattering studies of $CoPS_3$ are two other weaker intensity peaks, M_1' and M_2', which are centered at energies $\omega'_{M_1} = 106$ cm^{-1} and $\omega'_{M_2} = 186$ cm^{-1}, respectively. As shown in Fig. 2(a), the M_1' and M_2' peaks display pronounced energy shifts with the applied magnetic field: M_1' undergoes a redshift, while M_2' shows a blueshift. Moreover, the M_1'

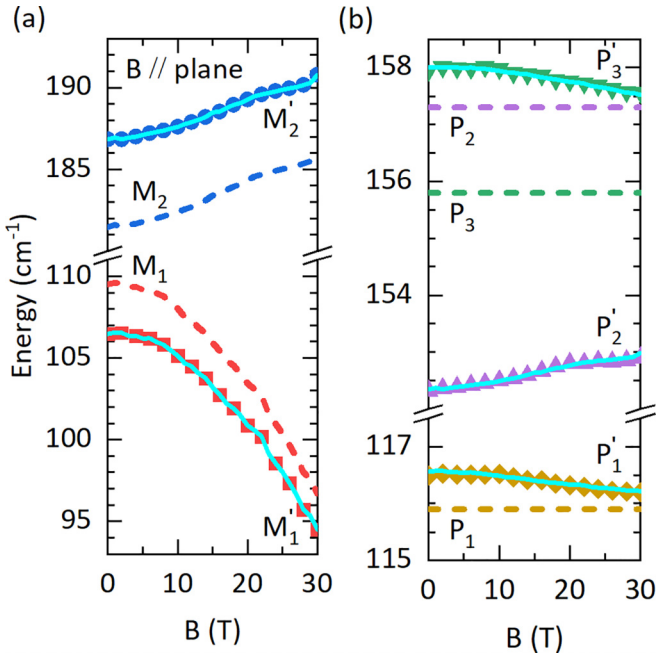

FIG. 3. The peak energies of the coupled (a) magnonlike modes (M_i') and (b) phononlike modes (P_i'), extracted from the in-plane magnetic-field dependence as presented in Fig. 2(a), are shown by solid symbols. Solid lines show the simulated magnetic-field dependence of coupled modes, while dashed lines indicate that of bare modes (M_i, P_i), both calculated using Eq. (2).

and M_2' resonances are considerably softened with increasing temperature and are hardly observed at temperatures above ~60 K [see Fig. 2(b)]. These characteristic behaviors point towards the magnon origin of the M_1' and M_2' modes. Notably, the energies of these modes (at $T = 5$ K, $B = 0$ T) are in reasonable agreement with those reported for the two low-energy magnon gap excitations observed in recent neutron scattering experiments [23].

A. Magnon-phonon coupling

In the following, we demonstrate that the observed Raman scattering modes are *de facto* not pure phonon or magnon excitations but represent the coupled magnon-phonon modes: P_1', P_2', and P_3' should be seen as phononlike modes, whereas M_1' and M_2' should be seen as magnonlike modes. The overall coupling scheme can already be deduced from the raw data shown in Fig. 2(a). Closer inspection of the data indicates that the application of the magnetic field not only affects the M_1' and M_2' modes but also leads to shifts, although weaker, of P_1', P_2', and P_3' resonances. This is emphasized in Fig. 3, where the energy positions of the observed Raman peaks are plotted as a function of the magnetic field. Markedly, the P_2' mode displays an upward shift with the magnetic field like the M_2' mode does, whereas the P_1' and P_3' modes experience downward shifts, following the field dependence of the M_1' mode. These observations direct us to the proposal of the selective magnon-phonon coupling in the $CoPS_3$ antiferromagnet: The P_2' and M_2' modes result from the coupling of the bare P_2 and M_2 modes, whereas the bare P_1 and P_3 modes couple to the bare M_1 mode. In line with the earlier approach [16,21] used to describe the selective magnon-phonon coupling in the $FePSe_3$ antiferromagnet, the following Hamiltonian is applied to reproduce the apparent energies of our coupled modes:

$$H_{5\times5} = \begin{bmatrix} \omega_{M_1} & \delta_1 & \delta_2 & 0 & 0 \\ \delta_1 & \omega_{P_1} & 0 & 0 & 0 \\ \delta_2 & 0 & \omega_{P_3} & 0 & 0 \\ 0 & 0 & 0 & \omega_{M_2} & \delta_3 \\ 0 & 0 & 0 & \delta_3 & \omega_{P_2} \end{bmatrix}. \quad (2)$$

Here, ω_{M_1} and ω_{M_1} correspond to the energies of the bare magnon modes M_1 and M_2, respectively. ω_{P_1}, ω_{P_2}, and ω_{P_3} correspond to the energies of the bare phonon modes P_1, P_2, and P_3, respectively. δ_1, δ_2, and δ_3 are the coupling parameters that control the hybridization of the M_1 magnon mode with the P_1 phonon mode, the M_1 magnon with the P_3 phonon, and the M_2 magnon with the P_2 phonon, respectively. Using this Hamiltonian, the eigenstates of the coupled magnon-phonon modes can be derived and eventually matched to those observed in the experiment. This procedure was applied to the entire ensemble of data points at different magnetic fields, as shown in Fig. 3 (see Sec. S3 of the SM [30]). To reproduce this set of data points, we assumed that the parameters δ_1, δ_2, δ_3, ω_{P_1}, ω_{P_2}, and ω_{P_3} are independent of the magnetic field while allowing the energies ω_{M_1} and ω_{M_2} of the bare magnon modes to vary with the field strength. The resulting data simulation is shown in Fig. 3. The measured energies of coupled modes are best reproduced when fixing $\delta_1 = 2.5 \pm 0.3$ cm^{-1}, $\delta_2 = 10.8 \pm 0.3$ cm^{-1}, $\delta_3 = 12.4 \pm 0.3$ cm^{-1}, $\omega_{P_1} = 115.9 \pm 0.3$ cm^{-1}, $\omega_{P_2} = 157.3 \pm 0.3$ cm^{-1}, and $\omega_{P_3} = 155.7 \pm 0.3$ cm^{-1} and the ω_{M_1} and ω_{M_2} dependences as shown in Fig. 3(a). At zero magnetic field, the energies of bare magnon modes are found to be ω_{M_1} ($B = 0$ T) $= 109.6 \pm 0.3$ cm^{-1} and ω_{M_2} ($B = 0$ T) $= 181.6 \pm 0.3$ cm^{-1}. Regarding the damping effects, the energy spacings of the coupled modes are significantly larger than the linewidths, and thus, non-Hermitian effects have a negligible impact on apparent gaps and the extracted parameters. The estimated magnon-phonon coupling coefficients (δ_2, δ_3) in $CoPS_3$ are significantly stronger than the values reported for other MPX_3 compounds (2–2.5 cm^{-1}) [14–16,21]. For $FePSe_3$, selective coupling has been attributed to the superposition of two orthogonal linear vibrations of degenerate phonon modes, which generate chirality and subsequently hybridize with chiral magnon modes [16]. In $CoPS_3$, however, the biaxial nature of the system gives rise to highly elliptical oscillations of the two magnon modes in orthogonal directions [31]. These elliptical magnon oscillations can couple to the linear vibrations of phonons, depending on their symmetry, thereby explaining the strong and selective character of the coupling coefficients.

Moreover, when setting the above values for the δ_i, ω_{P_i}, and ω_{M_i} ($B = 0$ T) parameters, we reproduce the evolution of the coupled modes measured as a function of the magnetic field applied along a different in-plane direction and along the out-of-plane direction (see Fig. 4). Notably, the extracted $\omega_{M_1}(B)$ and $\omega_{M_2}(B)$ dependences in the latter configurations differ from those obtained for the data shown in Fig. 3(a). The configuration-dependent B evolutions of the extracted

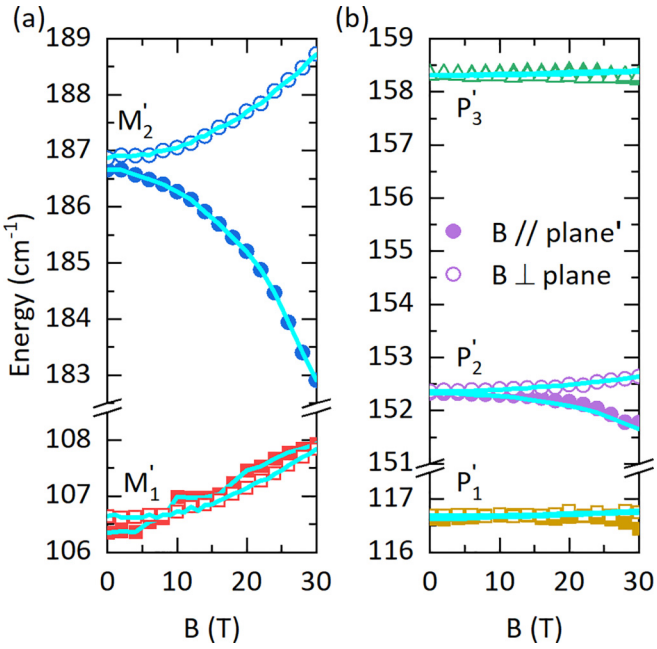

FIG. 4. Peak energies of (a) the magnonlike modes (M_i') and (b) the phononlike modes (P_i') as a function of the magnetic field applied along a different in-plane direction (solid symbols) and out-of-plane direction (open symbols). The false-color maps corresponding to these in-plane and out-of-plane magnetic-field dependences are presented in Figs. S2(d) and S3(a), respectively [30]. In this in-plane configuration, the magnetic field is applied along a crystal axis nearly orthogonal to that presented in Fig. 3. Solid lines display the simulated magnetic-field dependence of the coupled modes as calculated by solving Eq. (2).

bare magnon modes are discussed in the next section. At this point, we highlight the role of magnon-phonon coupling on the apparent positions of the phononlike P_2' and P_3' modes. Whereas the observed energy positions of these modes are $\omega_{P_2'} = 152$ cm^{-1} and $\omega_{P_3'} = 158$ cm^{-1}, their bare counterparts are almost degenerate at $\omega_{P_2} = 157$ cm^{-1} and $\omega_{P_3} = 156$ cm^{-1}, respectively. We therefore conclude that the observed separation ($\Delta = 6$ cm^{-1}) between the P_2' and P_3' modes is largely the result of the magnon-phonon coupling. It is a consequence of the remarkably strong coupling parameters $\delta_2 = 10.8$ cm^{-1} and $\delta_3 = 12.5$ cm^{-1}, even though the hybridizing bare magnon and phonon modes are quite separated in energy. Interestingly, our data modeling implies that the P_2' mode is located 6 cm^{-1} below the P_3' mode, whereas the energy ordering of their bare counterparts, P_2 and P_3 separated by 1 cm^{-1}, is inverted. The observed separation between the P_2' and P_3' modes measured in $CoPS_3$ at low temperatures was previously attributed to the effect of magnetostriction, possibly associated with the spin ordering phase. As discussed later, the magnetostriction could be the origin of the 1 cm^{-1} splitting, which we conclude for the bare P_2 and P_3 modes. Still, the observed 6 cm^{-1} separation between the apparent P_2' and P_3' modes is mainly due to magnon-phonon interaction.

Further insights into the low-energy excitations in $CoPS_3$ are gained by analyzing the Raman scattering spectra measured at different temperatures. Peak positions (energies at the maxima of peak intensities) of Raman scattering peaks extracted from the spectra illustrated in Fig. 2(b) are shown in Fig. 5(a). First, we focus on the temperature range $T =$ 5–60 K where all P_i' and M_i' peaks are visible in the spectra and simulate their energy positions following the proposed model of magnon-phonon coupling. We assume that the bare phonon modes and coupling coefficients are temperature independent in this temperature range and use the same set of parameters as specified above. As shown by the solid lines in Fig. 5(a), the experimental data are reasonably well reproduced, and we find that the energies of bare magnon modes exhibit softening with temperature according to the often encountered rule [32] $\omega_{M_i}(T) - \omega_{M_i}(T = 0\ K) \approx -T^{3.5}$ (see Fig. S5 of the SM [30]).

These magnon mode energies drop to zero at the Néel temperature, which implies that before reaching $T_N = 120$ K the M_2 mode crosses all phonon modes. The temperature evolution of the phononlike modes observed above $T =$ 60 K cannot be solely explained by our current model of magnon-phonon coupling, particularly in its assumption of temperature-independent bare phonon modes and coupling coefficients. The signatures of magnon-phonon coupling are, however, clearly visible, especially when we focus on the P_2' and P_3' resonances. This can be conveniently demonstrated when inspecting the P_2' and P_3' peaks in the polarization-resolved measurements [see Fig. 5(b)]. The Raman scattering spectra of $CoPS_3$ are known to follow the characteristic, linear-polarization selection rules [29] (see Fig. S1(b) of the SM [30]). In particular, the P_1', P_2', and M_2' modes are observed in the same linear polarization of the excitation laser, whereas the P_3' and M_1' modes appear in the orthogonal polarization. Peak positions (energies corresponding to the maxima of the peak intensities) and peak widths [full width at half maximum (FWHM)] are shown in Fig. 5(b). The temperature evolution of the energy separation ($\omega_{P_3'} - \omega_{P_2'}$) between the P_2' and P_3' peaks is plotted in Fig. 5(c), while the FWHM is shown in the inset. As can be seen in Fig. 5(b), at temperatures up to 80 K both the P_2' and P'_3 peaks display redshifts with temperature. The shift of the P_2' peak (induced by the M_2 magnon closely approaching the P_2 phonon) is, however, more pronounced than the shift of the P'_3 mode (which results from the increasing separation between the P_3 and M_1 modes). This explains the initial increase in ($\omega_{P_3'} - \omega_{P_2'}$) from 6 cm^{-1} (at 5 K) to 7 cm^{-1} (at 80 K), as illustrated in Fig. 5(c). The strong broadening of the P_2' peak, illustrated in the inset of Fig. 5(c), is observed at temperatures around 100 K, when the bare M_2 and P_2 modes are expected to overlap. This is another consequence of the magnon-phonon coupling in $CoPS_3$. When the temperature rises above 80 K, the separation between the P_3' and P_3' modes sharply decreases and drops to zero at 120 K. Shrinkage of ($\omega_{P_3'} - \omega_{P_2'}$) when approaching the paramagnetic phase, leading to the loss of the magnon resonances and the magnon-phonon coupling strength, is expected within our model of magnon-phonon hybridization. This model, however, does not explain the absence of the splitting between the P_2 and P_3 modes at $T = 120$ K or the actual energy position of the phonon modes observed at 120 K. Otherwise, they would be expected to correspond to the bare phonon modes, and in particular, we would expect to observe the 1 cm^{-1} splitting between the P_2 and P_3 peaks in the paramagnetic phase. In addition to the strong magnon-phonon coupling,

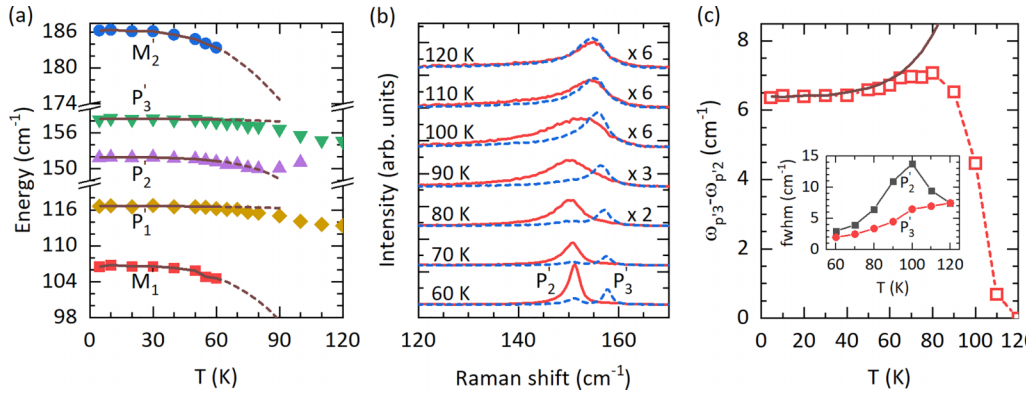

FIG. 5. (a) Peak energies of coupled modes as a function of temperature (solid symbols). The solid lines correspond to the simulated peak energies of the coupled modes calculated using Eq. (2). The bare magnon modes follow $-T^{3.5}$ dependence, as shown in Fig. S5 of the SM [30]. The extrapolated temperature dependence of the bare magnon modes is used to estimate the coupled mode energies at elevated temperatures, as shown by the dashed line. (b) Linear-polarization-resolved Raman scattering spectra highlighting the evolution of the P_2' and P_3' modes as a function of temperature below T_N. The solid red line denotes polarization parallel to the laser, whereas the dashed blue line represents polarization orthogonal to it. (c) The energy difference between the P_2' and P_3' modes as a function of temperature. The solid line corresponds to the energy difference obtained from the simulation. The full width at half maximum of the P_2' and P_3' modes as a function of temperature is shown in the inset.

other mechanisms, e.g., magnetostriction, likely exist which can create the 1 cm^{-1} splitting of the phonon resonances in the antiferromagnetic phase of $CoPS_3$.

B. Bare magnon modes

Having deconvoluted the uncoupled magnon modes, we proceed to analyze their energies and magnetic-field dependence with the aim of discussing the characteristic parameters governing spin ordering in the $CoPS_3$ antiferromagnet.

Since optical experiments specifically probe magnons with zero momentum ($k = 0$), we can replace the full spin Hamiltonian given in Eq. (1) with its truncated two-sublattice representation:

$$\hat{\mathcal{H}}_2 = J_{\text{eff}}\,\mathbf{S}_1 \cdot \mathbf{S}_2 + \hat{\mathcal{H}}_a - \mu_B \sum_{i=1}^{2} g_\alpha B^\alpha S_i^\alpha. \tag{3}$$

For further details on such an approach see Ref. [33]. Here, $J_{\text{eff}} = J_1 + 4J_2 + 3J_3$ is the net antiferromagnetic coupling between two opposite spins, $\hat{\mathcal{H}}_a$ is the biaxial magnetic anisotropy (1), and the last term is the Zeeman energy $\hat{\mathcal{H}}_Z$ written in the principal axis coordinate frame. Using the microscopic exchange parameters determined in [23], we estimate $J_{\text{eff}} \approx 7.99$ meV. We use the Holstein-Primakoff representation for the $S = 3/2$ spin operators to compute the $k = 0$ modes described by $\hat{\mathcal{H}}_2$ in zero and finite magnetic fields.

In zero field ($B = 0$ T), the two magnon gaps are expressed as

$$\begin{aligned}\omega_{M_1} &= 2S\sqrt{(-2E)(J_{\text{eff}} + D - E)},\\ \omega_{M_2} &= 2S\sqrt{(D - E)(J_{\text{eff}} - 2E)}.\end{aligned} \tag{4}$$

Using the microscopic constants from Ref. [23], we obtain $\omega_{M_1} = 115$ cm^{-1} and $\omega_{M_2} = 195$ cm^{-1}, which are larger than the values of 109.6 and 181.6 cm^{-1} determined experimentally in our work. In order to refine the microscopic constants, we use the full magnetic-field dependence of the bare magnon modes.

For a magnetic field perpendicular to the easy x axis, spins form a canted antiferromagnetic structure. For $B \parallel z$, the magnon gaps ω_{M_1} and ω_{M_2} are expressed as

$$\begin{aligned}\omega_{M_1} &= 2S\cos\theta\sqrt{(-2E)(J_{\text{eff}} + D - E)},\\ \omega_{M_2} &= 2S\sqrt{(J_{\text{eff}} - 2E)[J_{\text{eff}}\sin^2\theta + (D - E)\cos^2\theta]},\end{aligned} \tag{5}$$

where the canting angle θ is given by

$$\sin\theta = \frac{g_z\mu_B B}{2S(J_{\text{eff}} + D - E)}. \tag{6}$$

Similar expressions for $B \parallel y$ are

$$\begin{aligned}\omega_{M_1} &= 2S\sqrt{(J_{\text{eff}} + D - E)(J_{\text{eff}}\sin^2\theta - 2E\cos^2\theta)},\\ \omega_{M_2} &= 2S\cos\theta\sqrt{(D - E)(J_{\text{eff}} - 2E)},\end{aligned} \tag{7}$$

with

$$\sin\theta = \frac{g_y\mu_B B}{2S(J_{\text{eff}} - 2E)}. \tag{8}$$

Finally, for the $B \parallel x$ configuration, spins preserve the up-down collinear structure until the spin-flop transition. Since the corresponding field is not reached in our experiments, we present only the results for the collinear state:

$$\begin{aligned}\omega_{M_{1,2}}^2 = {} & (J_{\text{eff}} + D - 3E)^2S^2 - J_{\text{eff}}^2S^2 - (D + E)^2S^2\\ & + (g_x\mu_B B)^2 \pm 2S\big[J_{\text{eff}}^2(D + E)^2S^2\\ & + (g_x\mu_B B)^2(D - 3E)(2J_{\text{eff}} + D - 3E)\big]^{1/2}.\end{aligned} \tag{9}$$

Even though the microscopic parameters reported in Ref. [23] do not reproduce the magnon gap energies, the trend of the in-plane magnetic-field dependence of the ω_{M_1} and ω_{M_2} modes, as obtained using Eqs. (7)–(9) and shown in Fig. S6

TABLE I. Magnon-phonon coupling constants, bare magnon mode energies, and the magnetic interaction parameters of $CoPS_3$. A conversion factor of 1 $cm^{-1} = 0.124$ meV is used to express all parameters in the same units.

	δ_1 (meV)	δ_2 (meV)	δ_3 (meV)	ω_{P_1} (meV)	ω_{P_2} (meV)	ω_{P_3} (meV)	ω_{M_1} (meV)	ω_{M_2} (meV)	J_{eff} (meV)	D (meV)	E (meV)	g_x	g_y	g_z
Our work	0.3	1.4	1.6	14.8	19.6	19.5	13.7	22.8	9.9	4.3	−0.7	2	2	4
Ref. [23]							14.28	24.13	7.99	6.07	−0.77			

of the SM [30], confirms that the in-plane magnetic field is predominantly oriented along the magnetic x axis in Fig. 3 and along the magnetic y axis in Fig. 4. To refine the microscopic parameters (J_{eff}, D, and E), we used Eq. (4) for the magnon gaps and the out-of-plane magnetic-field dependence ($B \perp$ the plane) of the M_2 mode [Eq. (5)], treating them as three constraints. Here, we assume that the magnetic field remains perpendicular to the spin direction (even though it is canted by 10° along the out-of-plane direction). The resulting parameters obtained by solving these equations (see Sec. 5 of the SM [30]) are listed in Table I. The g factor along the magnetic z axis is found to be 4 ($g_z = 4$). The theoretical field dependence of the magnon gaps, using this set of parameters, is shown by solid lines in Figs. 6(a)–6(c), along with the experimental results (shown by symbols). The theoretical curves reproduce the experimental trends reasonably well for in-plane configurations of the magnetic field when the g factors are taken to be $g_x = 2$ and $g_y = 2$.

Notable deviations, particularly for the M_1 mode under $B \parallel z$ axis and at higher magnetic fields, may arise from several factors. First, even in the out-of-plane configuration ($B \parallel z$ axis), the field is not exactly orthogonal to the spin direction, introducing uncertainty into the parameter estimation. Similar misalignments are possible in the in-plane configurations, where the applied field may deviate from the exact magnetic axes. Furthermore, discrepancies may also originate from additional terms in the spin Hamiltonian that are not currently included in the theoretical model for $CoPS_3$. For example, the low monoclinic symmetry $C2/m$ at the Co site can lead to the following term in the crystal field Hamiltonian:

$$\hat{\mathcal{H}}'_a = K \sum_i \left(S_i^x S_i^z + S_i^z S_i^x\right). \tag{10}$$

This term causes Co spins to move out of the ab plane at zero magnetic field. Such a tilt of about 10° was experimentally observed in the neutron diffraction study of $CoPS_3$ [24]. Computing the tilting angle by minimizing $\hat{\mathcal{H}}_a + \hat{\mathcal{H}}'_a$ yields $K \simeq 0.18(D + |E|)$, which is comparable to other anisotropy parameters. The magnetic field applied perpendicular to the plane is also not along the magnetic z axis of $CoPS_3$. For magnetic fields up to 30 T, both the sublattice spins are expected to cant by about 10° for $B \parallel z$ axis, as can be obtained with Eq. (5). However, in the presence of comparable zero-field tilting, the field-dependent canting is different for the two sublattice spins. A detailed numerical solution is thus required to reproduce experimentally the observed magnetic-field dependence of the magnon modes, which is beyond the scope of this work.

Recently, we became aware of a related study [34] that investigates spin-lattice entanglement in $CoPS_3$ via temperature-dependent Raman scattering.

IV. CONCLUSIONS

In conclusion, the Raman scattering study revealed exceptionally strong and selective hybridization between magnons and phonons in the $CoPS_3$ antiferromagnet. A striking manifestation of this coupling is the pronounced splitting of two phononlike modes observed at 152 and 158 cm^{-1} in the antiferromagnetic phase, despite their nearly degenerate bare phonon origins. By modeling the extracted bare magnon modes and their magnetic-field dependences within existing theoretical frameworks, we proposed an updated set of effective exchange and magnetic anisotropy parameters that refine our understanding of spin ordering and dynamics in $CoPS_3$.

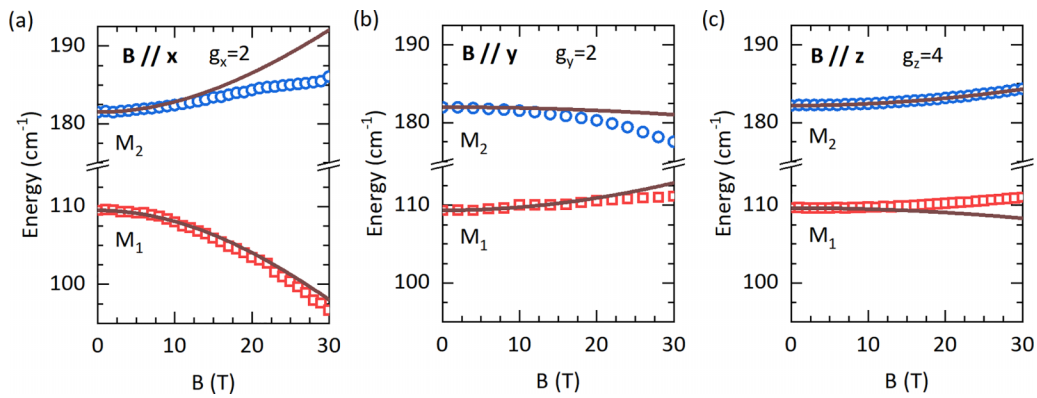

FIG. 6. (a)–(c) The theoretical evolution of magnon modes (M_1, M_2) as a function of magnetic field applied along the magnetic x, y, and z axes, respectively (solid lines). The exchange and anisotropy parameters are considered to be $J_{\text{eff}} = 9.9$ meV, $D = 4.3$ meV, and $E = -0.7$ meV, and the g factors are $g_x = 2$, $g_y = 2$, and $g_z = 4$. The bare magnon mode energies obtained for the magnetic-field configurations, presented in Figs. 3(a) and 4(a), are also shown in the respective plots (open symbols).

Our findings corroborate the strong anisotropy of the g factor in $CoPS_3$.

ACKNOWLEDGMENTS

Numerous valuable discussions with A. Wildes are acknowledged. The support of LNCMI-CNRS, a member of the European Magnetic Field Laboratory (EMFL), is acknowledged. M.P. acknowledges support from the European Union (ERC TERAPLASM No. 101053716) and the CENTERA2 FENG.02.01-IP.05-T004/23 project funded within the IRA program of the FNP Poland, cofinanced by the EU FENG Program. R.S. acknowledges the financial support provided by the Ministry of Science and Technology in Taiwan under Projects No. NSTC-113-2124-M-001-003 and No. NSTC-113-2112M001045-MY3, as well as support from Academia Sinica for the budget of AS-iMATE11412. M.K. acknowledges support from the Ministry of Education (Singapore) through the Research Centre of Excellence program (Grant No. EDUN C-33-18-279-V12, I-FIM), Academic Research Fund Tier 2 (Grant No. MOE-T2EP50122-0012), and the Air Force Office of Scientific Research and the Office of Naval Research Global under Award No. FA8655-21-1-7026.

DATA AVAILABILITY

The data that support the findings of this article are not publicly available. The data are available from the authors upon reasonable request.

[1] D. A. Bozhko, V. I. Vasyuchka, A. V. Chumak, and A. A. Serga, Magnon-phonon interactions in magnon spintronics, Low Temp. Phys. **46**, 383 (2020).

[2] K. Wang, K. Ren, Y. Hou, Y. Cheng, and G. Zhang, Magnon–phonon coupling: From fundamental physics to applications, Phys. Chem. Chem. Phys. **25**, 21802 (2023).

[3] P. Delugas, O. Baseggio, I. Timrov, S. Baroni, and T. Gorni, Magnon-phonon interactions enhance the gap at the Dirac point in the spin-wave spectra of CrI_3 two-dimensional magnets, Phys. Rev. B **107**, 214452 (2023).

[4] S. Streib, N. Vidal-Silva, K. Shen, and G. E. W. Bauer, Magnon-phonon interactions in magnetic insulators, Phys. Rev. B **99**, 184442 (2019).

[5] D. Shin, H. Hübener, U. De Giovannini, H. Jin, A. Rubio, and N. Park, Phonon-driven spin- Floquet magneto-valleytronics in MoS_2, Nat. Commun. **9**, 638 (2018).

[6] H. Man, Z. Shi, G. Xu, Y. Xu, X. Chen, S. Sullivan, J. Zhou, K. Xia, J. Shi, and P. Dai, Direct observation of magnon-phonon coupling in yttrium iron garnet, Phys. Rev. B **96**, 100406(R) (2017).

[7] P. Dai, H. Y. Hwang, J. Zhang, J. A. Fernandez-Baca, S.-W. Cheong, C. Kloc, Y. Tomioka, and Y. Tokura, Magnon damping by magnon-phonon coupling in manganese perovskites, Phys. Rev. B **61**, 9553 (2000).

[8] T. P. Lyons, J. Puebla, K. Yamamoto, R. S. Deacon, Y. Hwang, K. Ishibashi, S. Maekawa, and Y. Otani, Acoustically driven magnon-phonon coupling in a layered antiferromagnet, Phys. Rev. Lett. **131**, 196701 (2023).

[9] Y. Li, C. Zhao, W. Zhang, A. Hoffmann, and V. Novosad, Advances in coherent coupling between magnons and acoustic phonons, APL Mater. **9**, 060902 (2021).

[10] J. Holanda, D. Maior, A. Azevedo, and S. Rezende, Detecting the phonon spin in magnon–phonon conversion experiments, Nat. Phys. **14**, 500 (2018).

[11] H. T. Simensen, R. E. Troncoso, A. Kamra, and A. Brataas, Magnon-polarons in cubic collinear antiferromagnets, Phys. Rev. B **99**, 064421 (2019).

[12] K. Wang, J. He, M. Zhang, H. Wang, and G. Zhang, Magnon–phonon interaction in antiferromagnetic two-dimensional MXenes, Nanotechnology **31**, 435705 (2020).

[13] J. Li, H. T. Simensen, D. Reitz, Q. Sun, W. Yuan, C. Li, Y. Tserkovnyak, A. Brataas, and J. Shi, Observation of magnon polarons in a uniaxial antiferromagnetic insulator, Phys. Rev. Lett. **125**, 217201 (2020).

[14] D. Vaclavkova, M. Palit, J. Wyzula, S. Ghosh, A. Delhomme, S. Maity, P. Kapuscinski, A. Ghosh, M. Veis, M. Grzeszczyk, C. Faugeras, M. Orlita, S. Datta, and M. Potemski, Magnon polarons in the van der Waals antiferromagnet $FePS_3$, Phys. Rev. B **104**, 134437 (2021).

[15] S. Liu, A. G. del Aguila, D. Bhowmick, C. K. Gan, T. T. H. Do, M. A. Prosnikov, D. Sedmidubsky, Z. Sofer, P. C. M. Christianen, P. Sengupta, and Q. Xiong, Direct observation of magnon-phonon strong coupling in two-dimensional antiferromagnet at high magnetic fields, Phys. Rev. Lett. **127**, 097401 (2021).

[16] J. Cui, E. V. Bostroem, M. Ozerov, F. Wu, Q. Jiang, J.-H. Chu, C. Li, F. Liu, X. Xu, A. Rubio, and Q. Zhang, Chirality selective magnon-phonon hybridization and magnon-induced chiral phonons in an atomically thin antiferromagnet, Nat. Commun. **14**, 3396 (2023).

[17] T. T. Mai, K. F. Garrity, A. McCreary, J. Argo, J. R. Simpson, V. Doan-Nguyen, R. V. Aguilar, and A. R. H. Walker, Magnon-phonon hybridization in 2D antiferromagnet $MnPSe_3$, Sci. Adv. **7**, eabj3106 (2021).

[18] D. Vaclavkova, A. Delhomme, C. Faugeras, M. Potemski, A. Bogucki, J. Suffczyński, P. Kossacki, A. R. Wildes, B. Grémaud, and A. Saúl, Magnetoelastic interaction in the two-dimensional magnetic material $MnPS_3$ studied by first principles calculations and Raman experiments, 2D Mater. **7**, 035030 (2020).

[19] J. Luo, S. Li, Z. Ye, R. Xu, H. Yan, J. Zhang, G. Ye, L. Chen, D. Hu, X. Teng *et al.*, Evidence for topological magnon–phonon hybridization in a 2D antiferromagnet down to the monolayer limit, Nano Lett. **23**, 2023 (2023).

[20] A. Pawbake, T. Pelini, A. Delhomme, D. Romanin, D. Vaclavkova, G. Martinez, M. Calandra, M.-A. Measson, M. Veis, M. Potemski, M. Orlita, and C. Faugeras, High-pressure tuning of magnon-polarons in the layered antiferromagnet $FePS_3$, ACS Nano **16**, 12656 (2022).

[21] D. Jana, P. Kapuscinski, A. Pawbake, A. Papavasileiou, Z. Sofer, I. Breslavetz, M. Orlita, M. Potemski, and C. Faugeras, In-plane anisotropy in the van der Waals antiferromagnet $FePSe_3$ probed by magneto-Raman scattering, Phys. Rev. B **108**, 144415 (2023).

[22] B. Ilyas, T. Luo, A. von Hoegen, E. V. Boström, Z. Zhang, J. Park, J. Kim, J.-G. Park, K. A. Nelson, A. Rubio *et al.*, Terahertz field-induced metastable magnetization near criticality in $FePS_3$, Nature (London) **636**, 609 (2024).

[23] A. R. Wildes, B. Fåk, U. B. Hansen, M. Enderle, J. R. Stewart, L. Testa, H. M. Rønnow, C. Kim, and J.-G. Park, Spin wave spectra of single crystal $CoPS_3$, Phys. Rev. B **107**, 054438 (2023).

[24] A. R. Wildes, V. Simonet, E. Ressouche, R. Ballou, and G. J. McIntyre, The magnetic properties and structure of the quasi-two-dimensional antiferromagnet $CoPS_3$, J. Phys.: Condens. Matter **29**, 455801 (2017).

[25] C. Kim, J. Jeong, P. Park, T. Masuda, S. Asai, S. Itoh, H.-S. Kim, A. Wildes, and J.-G. Park, Spin waves in the two-dimensional honeycomb lattice XXZ-type van der Waals antiferromagnet $CoPS_3$, Phys. Rev. B **102**, 184429 (2020).

[26] A. R. Wildes, B. Fåk, U. B. Hansen, A. Ivanov, M. Enderle, and L. P. Peláez, Interplanar magnetic exchange in $CoPS_3$, J. Phys.: Condens. Matter **37**, 235804 (2025).

[27] K. Momma and F. Izumi, *Vesta 3* for three-dimensional visualization of crystal, volumetric and morphology data, J. Appl. Crystallogr. **44**, 1272 (2011).

[28] K. W. H. Stevens, Spin Hamiltonians, in *Magnetism*, edited by G. T. Rado and H. Suhl (Academic, New York, 1963), Vol. 1, pp. 1–23.

[29] Q. Liu, L. Wang, Y. Fu, X. Zhang, L. Huang, H. Su, J. Lin, X. Chen, D. Yu, X. Cui, J.-W. Mei, and J.-F. Dai, Magnetic order in XY-type antiferromagnetic monolayer $CoPS_3$ revealed by Raman spectroscopy, Phys. Rev. B **103**, 235411 (2021).

[30] See Supplemental Material at http://link.aps.org/supplemental/10.1103/8f92-lt57 for details on temperature- and linear-polarization-resolved Raman scattering, the magnetic-field dependence of magnon branches, the estimation of the magnon-phonon coupling constant, and the microscopic magnetic parameters.

[31] S. M. Rezende, A. Azevedo, and R. L. Rodríguez-Suárez, Introduction to antiferromagnetic magnons, J. Appl. Phys. **126**, 151101 (2019).

[32] U. Köbler, Bosonic and magnonic magnon dispersions, J. Magn. Magn. Mater. **502**, 166533 (2020).

[33] C. W. Cho, A. Pawbake, N. Aubergier, A. L. Barra, K. Mosina, Z. Sofer, M. E. Zhitomirsky, C. Faugeras, and B. A. Piot, Microscopic parameters of the van der Waals CrSBr antiferromagnet from microwave absorption experiments, Phys. Rev. B **107**, 094403 (2023).

[34] T. T. Mai, A. McCreary, K. F. Garrity, R. L. Dally, S. Shah, B. C. Chakoumakos, M. N. A. Taj, J. W. Lynn, M. A. McGuire, B. S. Conner, M. Zebarjadi, J. L. Musfeldt, A. R. H. Walker, R. Rao, and M. A. Susner, Spin-lattice entanglement in $CoPS_3$ [Phys. Rev. B (to be published)].